

# Computational aspects of growth-induced instabilities through eigenvalue analysis

A. Javili<sup>1</sup> · B. Dortdivanlioglu<sup>1</sup> · E. Kuhl<sup>2</sup> · C. Linder<sup>1</sup>

Received: 12 March 2015 / Accepted: 24 June 2015 / Published online: 14 July 2015  
© Springer-Verlag Berlin Heidelberg 2015

**Abstract** The objective of this contribution is to establish a computational framework to study growth-induced instabilities. The common approach towards growth-induced instabilities is to decompose the deformation multiplicatively into its growth and elastic part. Recently, this concept has been employed in computations of growing continua and has proven to be extremely useful to better understand the material behavior under growth. While finite element simulations seem to be capable of predicting the behavior of growing continua, they often cannot naturally capture the instabilities caused by growth. The accepted strategy to provoke growth-induced instabilities is therefore to perturb the solution of the problem, which indeed results in geometric instabilities in the form of wrinkles and folds. However, this strategy is intrinsically subjective as the user is prescribing the perturbations and the simulations are often highly perturbation-dependent. We propose a different strategy that is inherently suitable for this problem, namely *eigenvalue analysis*. The main advantages of eigenvalue analysis are that first, no arbitrary, artificial perturbations are needed and second, it is, in general, independent of the time step size. Therefore, the solution obtained by this methodology is not

subjective and thus, is generic and reproducible. Equipped with eigenvalue analysis, we are able to compute precisely the critical growth to initiate instabilities. Furthermore, this strategy allows us to compare different finite elements for this family of problems. Our results demonstrate that linear elements perform strikingly poorly, as compared to quadratic elements.

**Keywords** Growth-induced instabilities · Eigenvalue analysis · Morphological instabilities · Wrinkling

## 1 Introduction

Growth-induced instabilities are important mechanisms in the evolution of bio-materials [37]. Typical examples in living systems range from undesired folding in asthmatic airways [11, 20, 41] via wrinkling in skin [55], to desired cortical folding in mammalian brains [8, 48]. Buckling of a stiff layer on a soft compliant substrate is a classical example [1, 5] with several recent applications in electronic skin [58], stretchable electronics [30, 32] and material characterization [22]. This problem and variants thereof has been widely studied lately [7, 9, 10, 25, 26, 31, 53, 64].

Continuum approaches towards the formation of growth-induced instabilities in soft materials typically adopt the concept of finite growth [49]. The growth is coupled to deformation at the kinematic level using the multiplicative decomposition of the deformation gradient into an elastic and a growth part [54]. This concept requires the introduction of a fictitious intermediate configuration [21]. The intermediate configuration is stress-free and generally incompatible. The elastic part maps the intermediate configuration to the compatible deformed configuration on which boundary conditions are prescribed. Boundary conditions confine the

✉ C. Linder  
linder@stanford.edu

A. Javili  
ajavili@stanford.edu

B. Dortdivanlioglu  
berkin@stanford.edu

E. Kuhl  
ekuhl@stanford.edu

<sup>1</sup> Department of Civil and Environmental Engineering, Stanford University, Stanford, CA 94305, USA

<sup>2</sup> Department of Mechanical Engineering, Stanford University, Stanford, CA 94305, USA

domain and therefore, the growth induces *residual* stresses in the body that trigger instabilities [4, 29]. For further details on the continuum theory of growth and its implications see [12, 13, 15–17, 19, 21, 24, 34, 36, 65] and references therein. Note that we formulate the theory of growth within the framework of open system thermodynamic where the body is allowed to constantly exchange energetic structures [28] with its environment through fluxes across its boundary [14, 19].

This manuscript establishes a computational framework to study growth-induced instabilities using the finite element method. An accepted approach to provoke growth-induced instabilities is to prescribe perturbations such as nodal displacements or forces. However, this strategy is often highly perturbation-dependent. We argue that eigenvalue analysis is intrinsically suitable for this problem and show that it is precise and not subjective. Equipped with a strategy capable of computing the critical growth accurately, we then compare the performance of linear elements against quadratic elements. Our numerical studies demonstrate that linear elements perform strikingly poorly, as compared to quadratic elements.

The authors recognize that the idea of employing eigenvalue analysis to study the instabilities of a mechanical system is not radically new, see for instance [59, 63] and references therein. At the same time we feel that, with a growing interest in morphological instabilities and surface wrinkling of soft materials such as gels and biological tissues, this paper contributes to clarify some delicate issues concerning the onset of instabilities from a computational point of view. Within the context of growth-induced instabilities, eigenvalue analysis proves to be an efficient methodology to precisely compute the onset of wrinkling and compare the performance of different finite elements.

Also, it is rather well-established that quadratic elements outperform linear elements in capturing bending deformations and that quadratic elements are computationally more expensive than linear elements. Nevertheless, in most applications to date and benchmark examples such as Cook's membrane, the linear elements are adequate for compressible materials and are widely used. In morphological instabilities of soft materials though, linear elements are no longer acceptable since pronounced bending deformations play the dominant role in these problems. Our studies show that overall quadratic elements are remarkably more efficient than linear elements and shall be used in this context.

This manuscript is organized as follows. Section 2 deals with the theory of growth at finite strain. The notation and certain key concepts are introduced. In Sect. 3, we explain how the growth of a confined domain causes geometric instabilities in the form of wrinkles and folds. We introduce the key idea of this work, the application of eigenvalue analysis to capture growth-induced instabilities. Representative

examples are gathered in Sect. 4 where we illustrate the excellent performance of eigenvalue analysis and quadratic finite elements for both two-dimensional and three-dimensional studies. Section 5 concludes this work and provides further outlook and possible extensions.

## 2 Theory of growth at finite strain

### 2.1 Kinematics

Consider a continuum body that occupies the material configuration  $\mathcal{B}_0$  at time  $t = 0$ , as shown in Fig. 1. The non-linear orientation-preserving deformation  $\varphi$  maps  $\mathcal{B}_0$  to the spatial configuration  $\mathcal{B}_t$  at time  $t > 0$ . The corresponding linear map from the material to the spatial configuration is the deformation gradient defined as  $\mathbf{F} := \text{Grad}\varphi$ . The deformation gradient maps a material line element  $d\mathbf{X} \in T\mathcal{B}_0$  to a spatial line element  $d\mathbf{x} \in T\mathcal{B}_t$  via  $d\mathbf{x} = \mathbf{F} \cdot d\mathbf{X}$ . The Jacobian of the deformation gradient is defined by  $J := \det \mathbf{F}$  and indicates the change of a volume element due to the deformation.

The common approach to model volumetric growth [49] is to use the multiplicative decomposition of the deformation gradient  $\mathbf{F}$  into its elastic  $\mathbf{F}^e$  and growth,  $\mathbf{F}^g$  parts, see Fig. 2, as

$$\begin{aligned} \mathbf{F} &= \mathbf{F}^e \cdot \mathbf{F}^g \Rightarrow \mathbf{F}^e = \mathbf{F} \cdot \mathbf{F}^g{}^{-1} \quad \text{and} \\ J_e &= \det \mathbf{F}^e, \quad J_g = \det \mathbf{F}^g. \end{aligned} \quad (1)$$

The growth part  $\mathbf{F}^g$  maps the reference configuration  $\mathcal{B}_0$  to an intermediate configuration  $\mathcal{B}_g$  that is, in general, an incompatible configuration. The elastic part  $\mathbf{F}^e$  maps the intermediate configuration to the compatible spatial configuration. So, the free energy would be a function of only the elastic part  $\mathbf{F}^e$ . In what follows, the growth is assumed to be volumetric, homogeneous and independent of the deformation.

### 2.2 Growth models

In the case of *isotropic growth*, the volume of the body increases equally in all directions. Hence, the growth tensor,  $\mathbf{F}^g$  can be described by a single scalar growth parameter,  $g$  as

$$\mathbf{F}^g = \mathbf{I} + g \mathbf{I} = [1 + g] \mathbf{I}, \quad (2)$$

in which  $\mathbf{I}$  denotes the invariant identity tensor. Note, in the absence of the growth, i.e.  $g=0$ , the growth tensor  $\mathbf{F}^g = \mathbf{I}$ . The parameter  $g$  represents shrinkage or atrophy ( $g < 0$ ), no growth ( $g = 0$ ) and growth ( $g > 0$ ).

*Anisotropic growth* describes a situation where the volume of the body increases differently in different directions.

**Fig. 1** The material and spatial configurations of a continuum body with associated non-linear deformation map  $\varphi$  and the linear deformation map  $F = \text{Grad}\varphi$

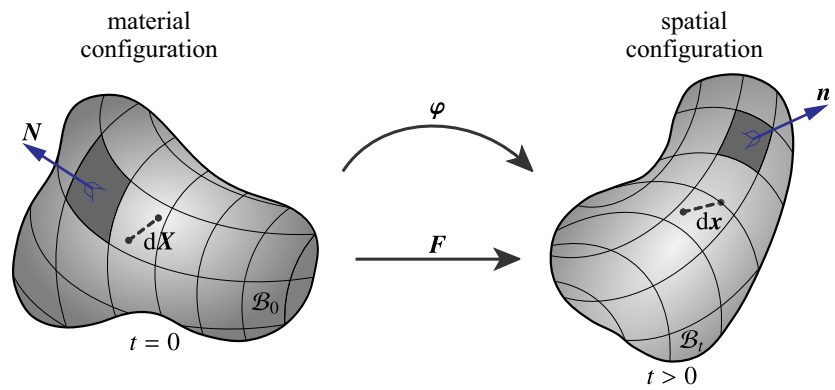
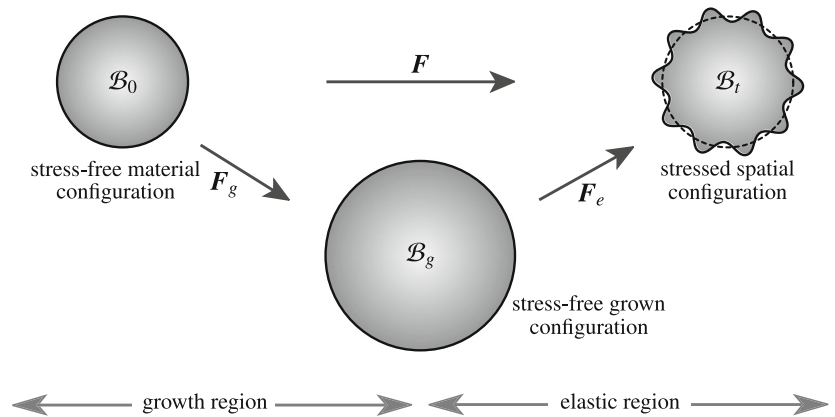


**Fig. 2** Illustration of kinematics of growth. The classical approach to model the growth is based on the multiplicative decomposition of the deformation gradient  $F$  into an elastic part  $F_e$  and a growth part  $F_g$ . The intermediate configuration  $B_g$  is, in general, incompatible



Therefore, the growth parameter shall be multiplied by a second-order tensor  $I_{\text{ani}}$  that represents the anisotropic growth behavior, resulting in

$$F_g = I + g I_{\text{ani}}. \tag{3}$$

We refer to  $I_{\text{ani}}$  as anisotropic identity. Next, consider the case in which the growth is transversely isotropic such that the material grows isotropically in a plane with the unit normal  $N$  but does not grow along the distinguished direction  $N$ . In this case  $I_{\text{ani}} = I - N \otimes N$  and the growth behavior is prescribed by

$$F_g = I + g [I - N \otimes N] = [1 + g] I - g N \otimes N. \tag{4}$$

For further details of anisotropic growth and its implications see [40].

### 2.3 Balance equations

The governing balance equations of finite strain continuum mechanics consist of the balance of linear and angular momentum. For a quasi-static process the balance of linear momentum in the domain  $B_0$  reads

$$\begin{aligned} \text{Div} P + b_0 &= 0 \quad \text{in } B_0 \quad \text{subject to} \\ P \cdot N &= t_0 \quad \text{on } \partial B_0, \end{aligned} \tag{5}$$

in which  $P$  denotes the Piola stress and  $b_0$  is the body force density in the material configuration. On the boundary of the domain the traction  $t_0$  is related to the Piola stress via the Cauchy theorem. In general,  $b_0$  and  $t_0$  are externally applied and prescribed in the problem definition. The balance of angular momentum, furnishes the condition

$$\begin{aligned} P \cdot F^t &= F \cdot P^t \quad \text{with} \quad P = \sigma \cdot \text{Cof} F \\ \Rightarrow \sigma &= \sigma^t, \end{aligned} \tag{6}$$

which essentially explains the symmetry of Cauchy stresses  $\sigma$ .

In order to obtain the weak form of the balance equations, the balance of linear momentum (5) is multiplied from the left with a test function  $\delta\varphi \in \mathcal{H}_0^1(B_0)$ . The result is integrated over the domain  $B_0$  and the divergence theorem is employed. The weak form of the balance of linear momentum reads

$$\int_{B_0} P : \text{Grad} \delta\varphi \, dV - \int_{B_0} \delta\varphi \cdot b_0 \, dV - \int_{\partial B_0} \delta\varphi \cdot t_0 \, dA = 0. \tag{7}$$

Finally, the weak form (7) is discretized using the finite element method. In particular, in this manuscript, linear and

quadratic elements are employed for the discretization and the results obtained from each type are compared.

### 2.4 Constitutive behavior

Constitutive models for soft materials are commonly proposed on a phenomenological [43] basis, which actually in [18] is shown to be related to a molecular statistic framework, or micromechanically justified [see [27,38,39,46,47,57] among many others]. Regardless of model origin, the response of those materials is prescribed by its free energy. The arguments of the free energy depend on the problem of interest. For the problem at hand, the deformation gradient  $\mathbf{F}$  and  $\mathbf{F}_g$  are the arguments of the (hyperelastic) free energy. Furthermore, since the intermediate configuration is assumed to be stress-free,  $\mathbf{F}_g$  does not explicitly contribute to the free energy. Therefore, the free energy density  $\psi(\mathbf{F}, \mathbf{F}_g)$  renders the same value as the elastic free energy  $\psi_e(\mathbf{F}_e)$ , i.e.

$$\psi = \psi(\mathbf{F}, \mathbf{F}_g) = \psi_e(\mathbf{F}_e). \tag{8}$$

On the other hand, the second law of thermodynamics and exploitation of the Coleman–Noll procedure relates the Piola stress to the free energy density in the material configuration by

$$\begin{aligned} \mathbf{P} &:= \frac{\partial \psi}{\partial \mathbf{F}} = \frac{\partial \psi_e}{\partial \mathbf{F}_e} : \frac{\partial \mathbf{F}_e}{\partial \mathbf{F}} = \frac{\partial \psi_e}{\partial \mathbf{F}_e} : [\mathbf{I} \overline{\otimes} \mathbf{F}_g^{-1}] \\ &= \mathbf{P}_e \cdot \mathbf{F}_g^{-1} \quad \text{with} \quad \mathbf{P}_e := \frac{\partial \psi_e}{\partial \mathbf{F}_e}. \end{aligned} \tag{9}$$

In deriving the Piola stress (9), the relation

$$\begin{aligned} \frac{\partial \mathbf{F}_e}{\partial \mathbf{F}} &= \frac{\partial (\mathbf{F} \cdot \mathbf{F}_g^{-1})}{\partial \mathbf{F}} = \mathbf{I} \overline{\otimes} \mathbf{F}_g^{-1} \quad \text{with} \\ [\mathbf{I} \overline{\otimes} \mathbf{F}_g^{-1}]_{ijkl} &= [\mathbf{I}]_{ik} [\mathbf{F}_g^{-1}]_{jl}, \end{aligned} \tag{10}$$

is utilized in which  $\overline{\otimes}$  denotes a non-standard tensor product. The non-standard tensor product  $\overline{\otimes}$  between two arbitrary second order tensors  $\mathbf{A}$  and  $\mathbf{B}$  in index notation can be represented as  $[\mathbf{A} \overline{\otimes} \mathbf{B}]_{ijkl} = [\mathbf{A}]_{ik} [\mathbf{B}]_{jl}$ .

The second derivative of the free energy density with respect to the deformation gradient is the fourth-order tensor  $\mathbb{A}$ . The tangent moduli  $\mathbb{A}$  is essential to compute the tangent stiffness of the finite element method.

$$\begin{aligned} \mathbb{A} &:= \frac{d}{d\mathbf{F}} \left( \frac{\partial \psi}{\partial \mathbf{F}} \right) = \frac{d\mathbf{P}}{d\mathbf{F}} = \frac{d(\mathbf{P}_e \cdot \mathbf{F}_g^{-1})}{d\mathbf{F}_e} : \frac{d\mathbf{F}_e}{d\mathbf{F}} \\ &= [\mathbf{I} \overline{\otimes} \mathbf{F}_g^{-1}] : \mathbb{A}_e : [\mathbf{I} \overline{\otimes} \mathbf{F}_g^{-1}] \quad \text{with} \\ \mathbb{A}_e &:= \frac{\partial \mathbf{P}_e}{\partial \mathbf{F}_e}. \end{aligned} \tag{11}$$

Here, the hyperelastic response of the matter is computed by a compressible neo-Hookean model with the free energy of the form

$$\begin{aligned} \psi_e &= \frac{1}{2} \mu [\mathbf{F}_e : \mathbf{F}_e - 3 - 2 \ln J_e] + \frac{1}{2} \lambda \left[ \frac{1}{2} [J_e^2 - 1] \right. \\ &\quad \left. - \ln J_e \right] \quad \text{with} \quad J_e = \det \mathbf{F}_e, \end{aligned} \tag{12}$$

in which  $\mu$  and  $\lambda$  are the Lamé material parameters. The corresponding elastic Piola stress  $\mathbf{P}_e$  and its derivative read

$$\mathbf{P}_e = \frac{\partial \psi_e}{\partial \mathbf{F}_e} = \mu [\mathbf{F}_e - \mathbf{F}_e^{-t}] + \frac{1}{2} \lambda [J_e^2 - 1] \mathbf{F}_e^{-t}, \tag{13}$$

$$\begin{aligned} \mathbb{A}_e &= \frac{\partial \mathbf{P}_e}{\partial \mathbf{F}_e} = \mu [\mathbb{I} - \mathbb{D}_e] + \frac{1}{2} \lambda [J_e^2 - 1] \mathbb{D}_e \\ &\quad + \lambda J_e^2 \mathbf{F}_e^{-t} \otimes \mathbf{F}_e^{-t} \quad \text{with} \quad \mathbb{I} := \mathbf{I} \overline{\otimes} \mathbf{I} \quad \text{and} \\ \mathbb{D}_e &:= -\mathbf{F}_e^{-t} \underline{\otimes} \mathbf{F}_e^{-1}, \end{aligned} \tag{14}$$

where  $\mathbb{I}$  denotes the fourth-order identity tensor and  $\mathbb{D}_e := \partial \mathbf{F}_e^{-t} / \partial \mathbf{F}_e = -\mathbf{F}_e^{-t} \underline{\otimes} \mathbf{F}_e^{-1}$  with  $[\mathbb{D}_e]_{ijkl} = -[\mathbf{F}_e^{-t}]_{il} [\mathbf{F}_e^{-1}]_{jk}$ .

Some applications of growing materials, such as bio-films, are suitable to be modeled as a plane strain problem due to their particular geometry and boundary conditions. A particular advantage of the choice of the free energy (12) is that it remains formally identical in the case of the plane strain.

### 3 Growth-induced instability

Consider a continuum body as shown in Fig. 3 constrained at some portions of its domain or on its surface through Dirichlet-type boundary conditions. When the body  $\mathcal{B}_0$  starts to grow, the confinement of the geometry initiates stresses inside the domain. The growth  $g$  continues until it reaches a critical value  $g_c$  at which the stresses are enough to induce geometric instabilities in the form of folding or wrinkling. Further growth increases the amplitude of the folds and could eventually cause secondary folding. In a discrete setting, this phenomenon can be illustrated by analyzing the tangent stiffness matrix associated with the finite element method. Let us first explore the meaning of the stiffness matrix within a non-linear finite element framework.

The goal of the finite element method is to solve the weak form (7). Within the non-linear finite element setting, the left-hand side of Eq. (7) is discretized using the finite elements and is denoted as a residual vector  $\mathbf{R}(\boldsymbol{\varphi})$ . For a detailed exposition on the non-linear finite element method, see for instance [61]. A vanishing residual vector is *approximately* equivalent to solving the non-linear system

$$\mathbf{R}(\boldsymbol{\varphi}) \stackrel{!}{=} \mathbf{0}. \tag{15}$$

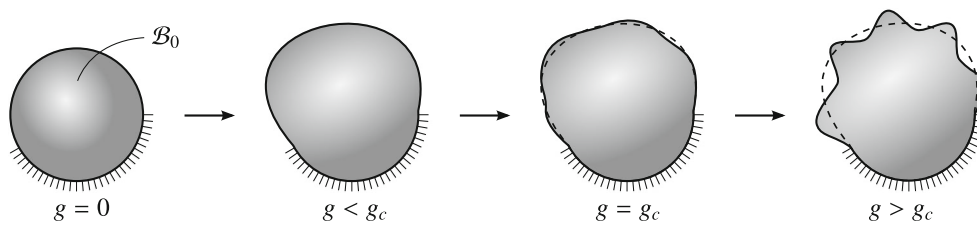


**Fig. 3** Formation of growth-induced instabilities. The configuration  $\mathcal{B}_0$  grows until it reaches a critical growth value  $g_c$  at which geometric instabilities in the form of wrinkles or folds occur. Further growth increases the folding amplitude, and may eventually induce secondary folding

In order to solve Eq. (15), i.e., to find  $\varphi$  such that  $\mathbf{R}$  vanishes, a Newton–Raphson scheme is utilized. The consistent linearization of the resulting system of equations yields

$$\begin{aligned} \mathbf{R}(\varphi) \stackrel{!}{=} \mathbf{0} &\Rightarrow \mathbf{R}(\varphi_{k+1}) \stackrel{!}{=} \mathbf{0} \quad \text{with} \\ \mathbf{R}(\varphi_{k+1}) &= \mathbf{R}(\varphi_k) + \left. \frac{\partial \mathbf{R}}{\partial \varphi} \right|_k \cdot \Delta \varphi \stackrel{!}{=} \mathbf{0} \quad \text{and} \\ \varphi_{k+1} &= \varphi_k + \Delta \varphi. \end{aligned} \tag{16}$$

The stiffness matrix  $\mathbf{K}$  is defined as the derivative of the residual with respect to deformation as  $\mathbf{K} := \partial \mathbf{R} / \partial \varphi$ . The eigenspace representation of the stiffness matrix of a system with  $n$  degrees of freedom (DOF) reads

$$\begin{aligned} \mathbf{K}_{n \times n} &= K_1 \lambda_1 \otimes \lambda_1 + K_2 \lambda_2 \otimes \lambda_2 + \dots + K_i \lambda_i \otimes \lambda_i \\ &+ \dots + K_n \lambda_n \otimes \lambda_n = \sum_{i=1}^n K_i \lambda_i \otimes \lambda_i, \end{aligned} \tag{17}$$

in which  $k_i$  and  $\lambda_i$  for  $i = 1, \dots, n$ , denote an eigenvalue and its associated *unit* eigenvector, respectively. This representation of the tangent stiffness is valid only in the case of diagonalizable matrices. All symmetric real stiffness matrices are diagonalizable. The constitutive response in Sect. 2.4 guarantees the symmetry of the tangent stiffness since growth is morphogenetic and independent of the deformation gradient. Hence, the stiffness is diagonalizable. For a more generic case where the growth is mechanically driven the tangent stiffness can become non-symmetric [35, 40] or even defective. The proposed methodology is essentially valid even for non-symmetric diagonalizable tangent stiffnesses in the sense that negative eigenvalues indicate unstable modes. The validity of the proposed scheme for general defective matrices has not been tested and is out of the scope of this manuscript.

Inserting the eigenspace representation of the stiffness into Eq. (16), yields

$$\mathbf{R}(\varphi) + \mathbf{K} \cdot \Delta \varphi \stackrel{!}{=} \mathbf{0} \Rightarrow \sum_{i=1}^n K_i \lambda_i \otimes \lambda_i \cdot \Delta \varphi = -\mathbf{R}. \tag{18}$$

Next, we represent the deformation increment  $\Delta \varphi$  and the residual  $\mathbf{R}$  in the eigenspace of the stiffness matrix of the system as

$$\Delta \varphi = \Delta \varphi_j \lambda_j \quad \text{and} \quad \mathbf{R} = R_r \lambda_r. \tag{19}$$

Replacing the relations (19) in Eq. (18) and using the orthogonality property of the eigenvectors, i.e.  $\lambda_i \cdot \lambda_j = \delta_{ij}$ , we obtain

$$K_i \Delta \varphi_i = R_i \quad \forall i \in \{1, \dots, n\} \quad (\text{no sum}). \tag{20}$$

Let,  $K_m$  ( $1 \leq m \leq n$ ) be the smallest positive eigenvalue of the stiffness matrix approaching zero due to increasing growth  $g$  and define the critical growth  $g_c$  exactly when the smallest eigenvalue reaches zero. The associated eigenvector  $\lambda_m$  is the geometric instability at  $g_c$ . Equipped with this knowledge, we devise two methodologies to capture growth-induced instabilities within the finite element framework.

• Prescribing perturbation

A common approach to capture growth-induced instabilities is to manually prescribe perturbations, see for instance [4, 45]. This method can be explained by referring to Eq. (20) as follows. Applying a very small perturbation to the system will lead to a very small residual and therefore each  $R_i$  assumes a non-vanishing value. Clearly, dividing the infinitesimal  $R_i$  by  $K_i$  yields a negligible deformation for all  $i$  except  $i = m$  that results in a finite value of  $\Delta \varphi_m$  when the growth is close enough to  $g_c$  and therefore,  $K_m$  is small enough. Note, the residual perturbation can either be achieved by prescribing a small perturbation to the displacement field or to the force field.

The advantage of prescribing perturbations, and perhaps the main reason for its popularity, is its simplicity. However, this methodology is, in general, not very accurate to compute the critical growth  $g_c$ . Also, it relies on the perturbation itself. For too small perturbations, growth can exceed its critical value without causing an instability. For too large perturbations, the perturbation itself may actually overwrite the solution. Due to the intrinsic numerical issues with this methodology, we propose another procedure based on the eigenvalue analysis that eliminates (subjective) perturbations.

• Eigenvalue analysis

The eigenvalue analysis provides a robust and reliable framework to capture growth-induced instabilities. It can

compute the critical growth precisely and is independent of the initial step size. Also, no perturbation is involved and therefore, eigenvalue analysis does not suffer from numerical issues. Its only drawback is that it requires the computation of eigenvalues, which could become computationally expensive. However, since we are only interested in a few small eigenvalues, efficient algorithms such as subspace iteration can be employed, see for instance [2,3,42].

In contrast to the first methodology that was built upon  $\mathbf{R}$  and  $\Delta\varphi$ , the eigenvalue analysis focuses on the stiffness  $\mathbf{K}$  itself. The eigenvalues  $K_i$  of the stiffness are calculated using an eigenvalue solver. If all eigenvalues are positive, growth is increased until one or multiple eigenvalues become negative. For instance, to compute the critical growth, the step size is adjusted until at least one negative eigenvalue within a defined tolerance from zero is obtained. Adjusting the step size can be done using a bi-section or secant method. Once the critical growth is reached with a certain tolerance, its associated eigenvector identifies the geometric instability pattern that we could have also obtained using carefully the perturbation of the first method.

In the numerical examples, we use bi-section to compute the critical growth. For all examples, we required less than 40 iterations to compute the critical growth with four digits of accuracy. To achieve the same accuracy by *prescribing perturbations* at least  $10^4$  increments are required provided that the perturbations are properly chosen. The eigenvalue analysis is more robust in the sense that it does not require any particular insight of the problem and the starting values for the bi-section can be chosen arbitrarily.

## 4 Representative examples

The objective of this section is to illustrate the nature of growth-induced instabilities using numerical examples. In particular, we study the influence of the mesh quality in terms

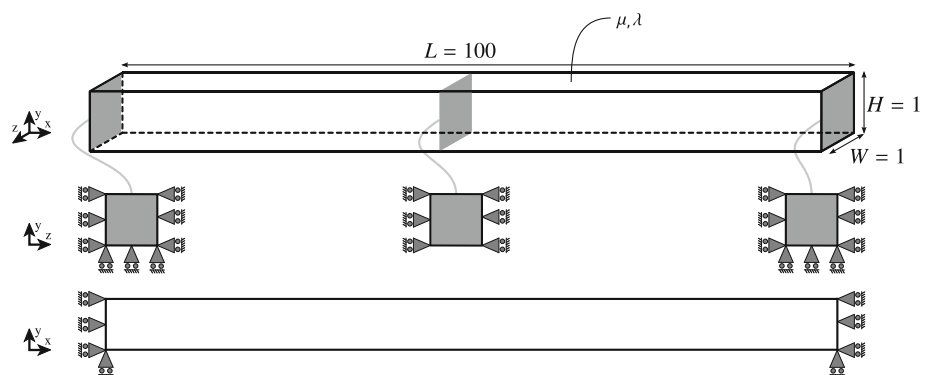
of element type and number of degrees of freedom. Furthermore, two different methodologies are employed to capture instabilities. In contrast to *prescribing a perturbation* that triggers instabilities, the eigenvalue analysis captures only the onset of instabilities and the deformation shown in the examples are the eigenvectors but not the actual deformation itself.

We conduct three case studies as follows. First, we perform a bifurcation analysis of a slender beam and show the superior behavior of quadratic elements compared to the linear ones. This example proves the ability and reliability of the proposed eigenvalue analysis to study growth-induced instabilities. We then show that using the results provided by the eigenvalue analysis, *prescribing perturbations* could capture higher instability modes and hence, the complete bifurcation tree. It is virtually impossible to observe such higher modes with perturbations if the critical eigenvalues are not available since the perturbations naturally converge to the very first mode. Next, we study a growing film on a soft substrate. Motivated by the first example, here we use quadratic elements and eigenvalue analysis. We provide accurate results that shall serve as benchmark numerical examples. The last example is a three-dimensional simulation of a growing layer on a compliant substrate. This example clearly proves the applicability of the eigenvalue analysis for a variety of problems regardless of the size and problem dimensions.

### 4.1 Bifurcation study of a growing slender beam

The first example of interest is the buckling analysis of a growing slender beam as shown in Fig. 4. The beam has a length of  $L = 100$  with a unit square cross section under plane-strain like conditions and grows only along its length. Therefore, it is modeled as a two-dimensional plane strain problem with the anisotropic growth tensor  $\mathbf{F}_g = \mathbf{I} + g \mathbf{e}_x \otimes \mathbf{e}_x$ . Figure 4 depicts the geometry of the domain and the prescribed boundary conditions. Clearly, the growth of the beam induces stresses along the beam resulting in instabilities. The slenderness of the beam, prescribed boundary conditions and the anisotropic growth

**Fig. 4** Geometry and boundary conditions of a growing beam



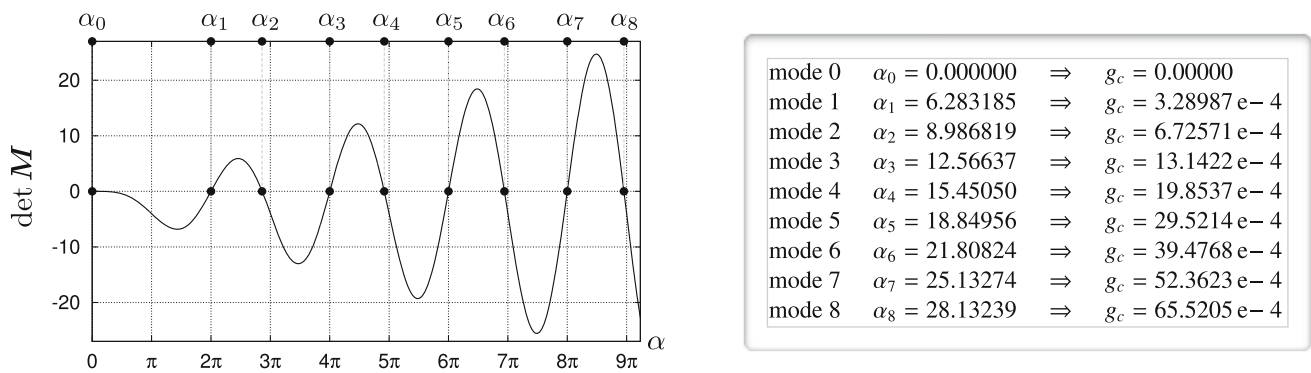


**Fig. 5** Illustration of  $\det M$  (left) and its roots (right). The roots are proportional to the square roots of the critical growth value, i.e.,  $\alpha \propto \sqrt{g_c}$

make our study comparable to the classical example of an Euler beam clamped at both ends. Therefore, the numerical results can be compared against the analytical solution in Sect. 4.1.1.

We study two cases of a fully compressible material ( $\nu = 0$ ) and a nearly incompressible material  $\nu = 0.49$  with  $\nu$  being the Poisson’s ratio. For the spatial discretization, we vary the number of elements along the length and across the height of the beam to study the mesh sensitivity of different element types.

#### 4.1.1 Analytical solution

We establish an analytical solution for the growing slender beam satisfying the assumptions associated with the Euler beam theory. Nevertheless, the influence of Poisson’s ratio on the results is negligible for this example. This is due to the slenderness of the beam, the anisotropic growth and the prescribed boundary condition, hence, very small values for critical growth. The governing differential equation for a growing beam with a square cross section of height  $H$  reads

$$\frac{\partial^4 w(x)}{\partial x^4} + \frac{12}{H^2} g \frac{\partial^2 w(x)}{\partial x^2} = 0 \quad \text{at } x = 0 : \quad w = \frac{\partial w}{\partial x} = 0 \quad \text{and} \quad \text{at } x = L : \quad w = \frac{\partial w}{\partial x} = 0, \quad (21)$$

where  $w(x)$  is the deflection in  $y$  direction and  $g$  indicates the anisotropic growth along the beam. The boundary conditions for a clamped-clamped beam are fixed deflections as well as fixed rotations at both ends. The general solution for the differential equation (21) is

$$w(x) = c_1 \sin(\beta x) + c_2 \cos(\beta x) + c_3 x + c_4 \quad \text{with} \quad \beta^2 = \frac{12}{H^2} g \Rightarrow \beta = 2 \frac{1}{H} \sqrt{3g}, \quad (22)$$

which by defining  $\alpha := L \beta$  can alternatively be expressed as

$$w(x) = c_1 \sin\left(\alpha \frac{x}{L}\right) + c_2 \cos\left(\alpha \frac{x}{L}\right) + c_3 x + c_4 \quad \text{with} \quad \alpha = 2 \frac{L}{H} \sqrt{3g}. \quad (23)$$

Prescribing the boundary conditions on the general solution (23) results in a system of 4 equations and 4 unknowns for which we seek for the non-trivial solution. The translational boundary conditions impose  $c_4 = -c_2$  and  $c_3 = -c_1 \alpha / L$  and therefore, reduce the system of equations to

$$\mathbf{M} \cdot \mathbf{c} = \mathbf{0} \quad \text{with} \quad \mathbf{M} = \begin{bmatrix} \sin \alpha - \alpha & \cos \alpha - 1 \\ \cos \alpha - 1 & -\sin \alpha \end{bmatrix} \quad \text{and} \quad \mathbf{c} = \begin{bmatrix} c_1 \\ c_2 \end{bmatrix}. \quad (24)$$

In order to obtain the non-trivial solution for the coefficients  $c_1$  and  $c_2$ , we set the determinant of  $\mathbf{M}$  to zero.

$$\det \mathbf{M} = \alpha \sin(\alpha) + 2 \cos(\alpha) - 2 \stackrel{!}{=} 0 \Rightarrow \det \mathbf{M} = \sin\left(\frac{\alpha}{2}\right) \left[ \alpha \cos\left(\frac{\alpha}{2}\right) - 2 \sin\left(\frac{\alpha}{2}\right) \right] \stackrel{!}{=} 0. \quad (25)$$

Therefore, the solutions of Eq. (25) are

$$\sin\left(\frac{\alpha}{2}\right) \stackrel{!}{=} 0 \Rightarrow \alpha = 2\pi, 4\pi, \dots \quad \text{or} \quad \tan\left(\frac{\alpha}{2}\right) \stackrel{!}{=} \frac{\alpha}{2} \Rightarrow \alpha = 8.9868, 15.4505, \dots, \quad (26)$$

illustrated in Fig. 5.

The solution of  $\det \mathbf{M} = 0$  indicates the critical growth values through the relation

$$g_c = \frac{1}{12} \left[ \frac{H}{L} \right]^2 \alpha^2, \quad (27)$$

function  $f(x)$  vs.  $x$  for  $0 \leq x \leq 100$  for different values of  $\alpha$

$$f(x) = \frac{1 - \cos \alpha}{\sin \alpha - \alpha} \left[ \sin \left( \alpha \frac{x}{L} \right) - \left( \alpha \frac{x}{L} \right) \right] + \cos \left( \alpha \frac{x}{L} \right) - 1$$

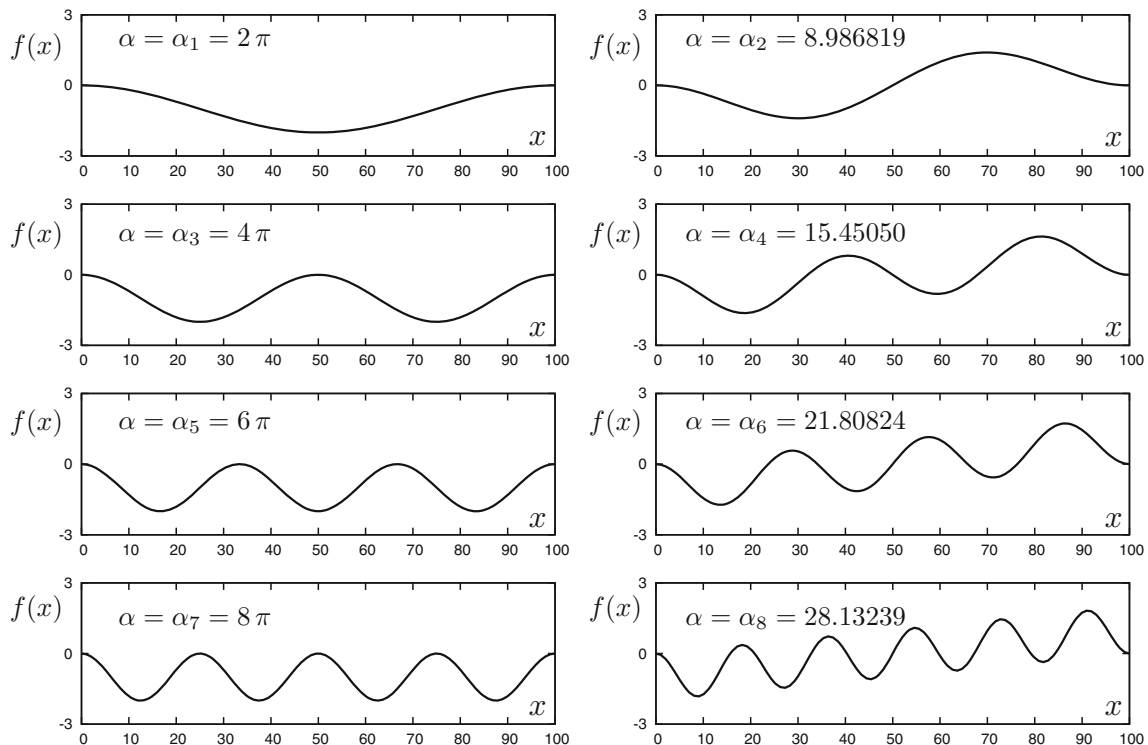


**Fig. 6** Analytical solution for the deformation of the beam according to Eq. (28). The values for  $\alpha$  are the roots of the equation (25). Note that for  $\alpha = 2\pi, 4\pi, \dots$ , the coefficient  $[1 - \cos \alpha]$  of the bracket vanishes identically resulting in a purely sinusoidal solution (left column)

from Eq. (23). For each critical  $\alpha$  the particular solution of the problem reduces to

$$\frac{w(x)}{c_2} = \frac{1 - \cos \alpha}{\sin \alpha - \alpha} \left[ \sin \left( \alpha \frac{x}{L} \right) - \left( \alpha \frac{x}{L} \right) \right] + \cos \left( \alpha \frac{x}{L} \right) - 1, \tag{28}$$

illustrated in Fig. 6. Note that the deflection of the beam for the right column in Fig. 6 is somewhat unexpected as it deviates from the purely sinusoidal solution. However, this solution follows naturally from the general solution (23) and the prescribed boundary conditions for this problem. The coefficients  $c_3$  and  $c_4$  corresponding to a linear and constant deformation, respectively, do not necessarily vanish for the both-end clamped beam of interest here. If the beam is simply supported (hinged) though, both  $c_3$  and  $c_4$  vanish identically resulting in a purely sinusoidal response. For a detailed exposition of elastic stability of beams, see [56].

#### 4.1.2 Numerical investigation by eigenvalue analysis

In order to study the performance of the eigenvalue analysis we compute the critical growth for the first eight eigenmodes of the slender beam. We perform both h- and p-adaptive sensitivity analysis. We explore the influence of Poisson’s ratio on the convergence behavior at  $\nu = 0$  and  $\nu = 0.49$ . The errors in Figs. 7 and 8 are computed with respect to the analytical solution and expressed in percentage. Analyzing the results, we draw the following conclusions.

First, linear elements are less accurate than the quadratic elements. Clearly, one quadratic element is computationally more expensive than that of the one linear element. However, the convergence behavior of quadratic elements is superior over linear elements. Therefore, numerical simulations based on quadratic elements are effectively computationally cheaper than the linear elements. Second, linear elements show strong locking behavior for  $\nu = 0.49$  although they perform slightly better for Poisson’s ratio  $\nu = 0$ . Even for  $\nu = 0$  only 60 quadratic elements outperform 4800 linear ele-

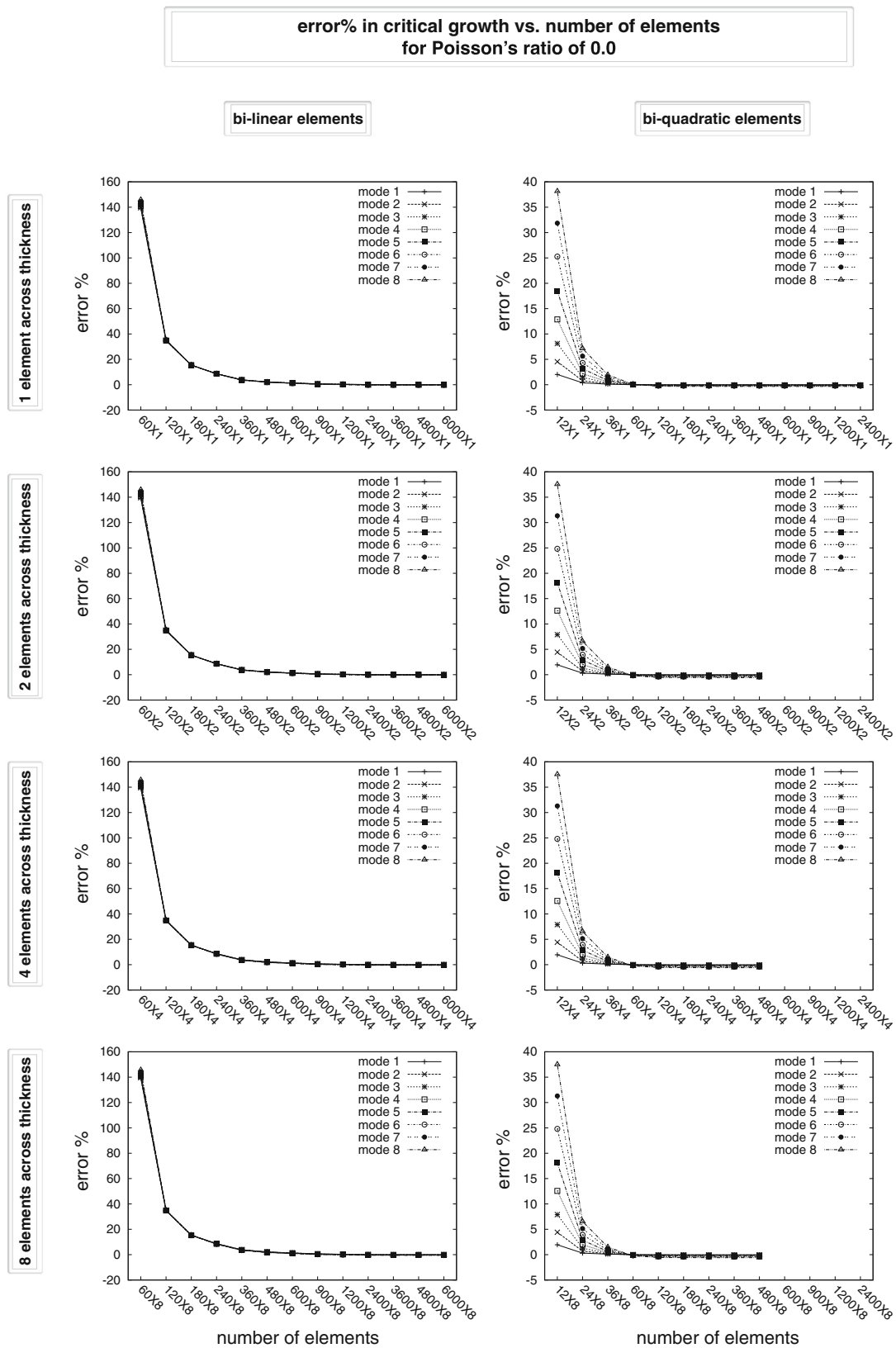


**Fig. 7** Error% versus number of elements for Poisson's ratio  $\nu = 0$ . Number of elements are indicated by  $p \times q$  where  $p$  indicates the number of elements along the beam and  $q$  the number of elements across its height

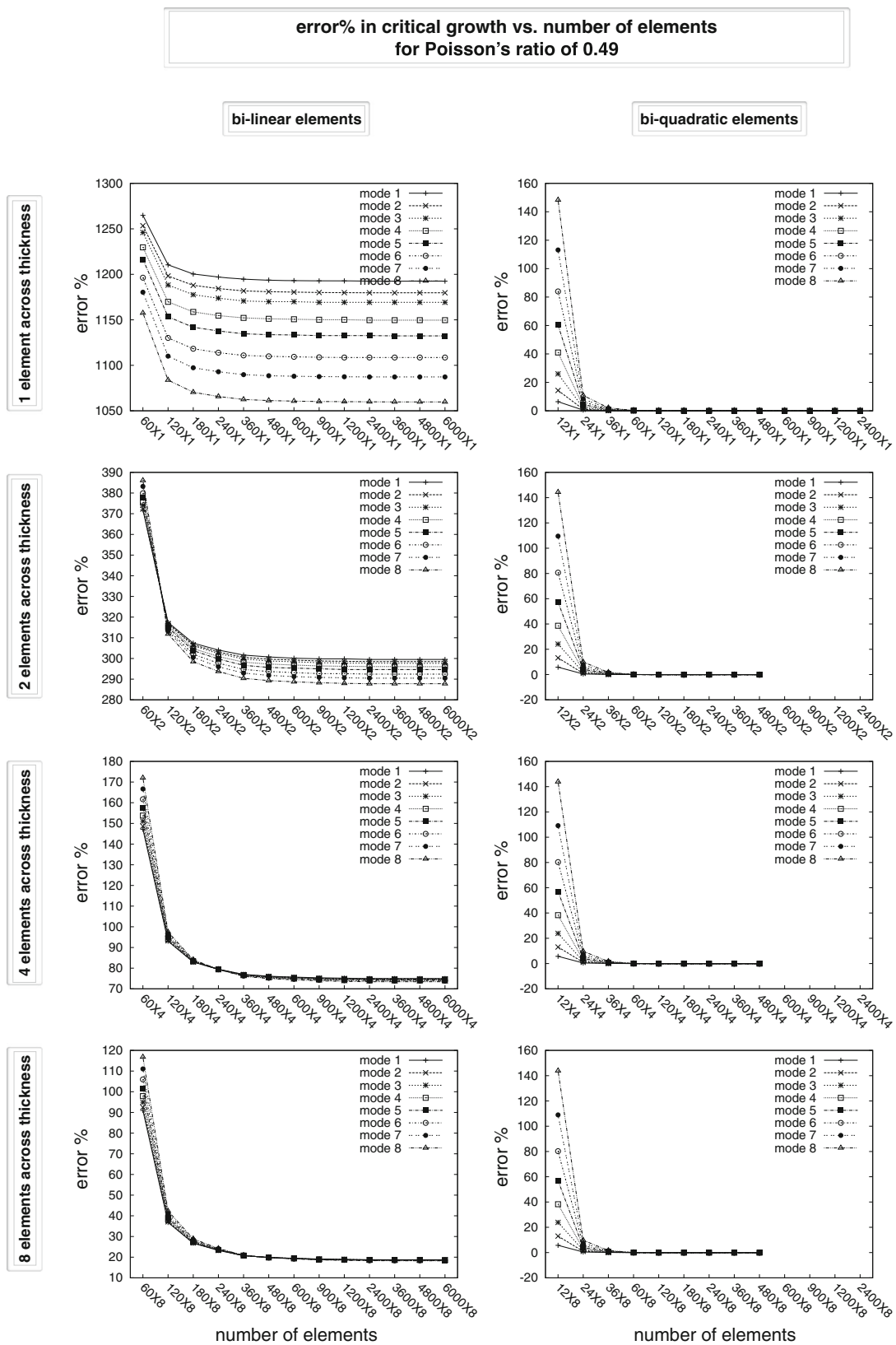


**Fig. 8** Error% versus number of elements for Poisson's ratio  $\nu = 0.49$ . Number of elements are indicated by  $p \times q$  where  $p$  indicates the number of elements along the beam and  $q$  the number of elements across its height

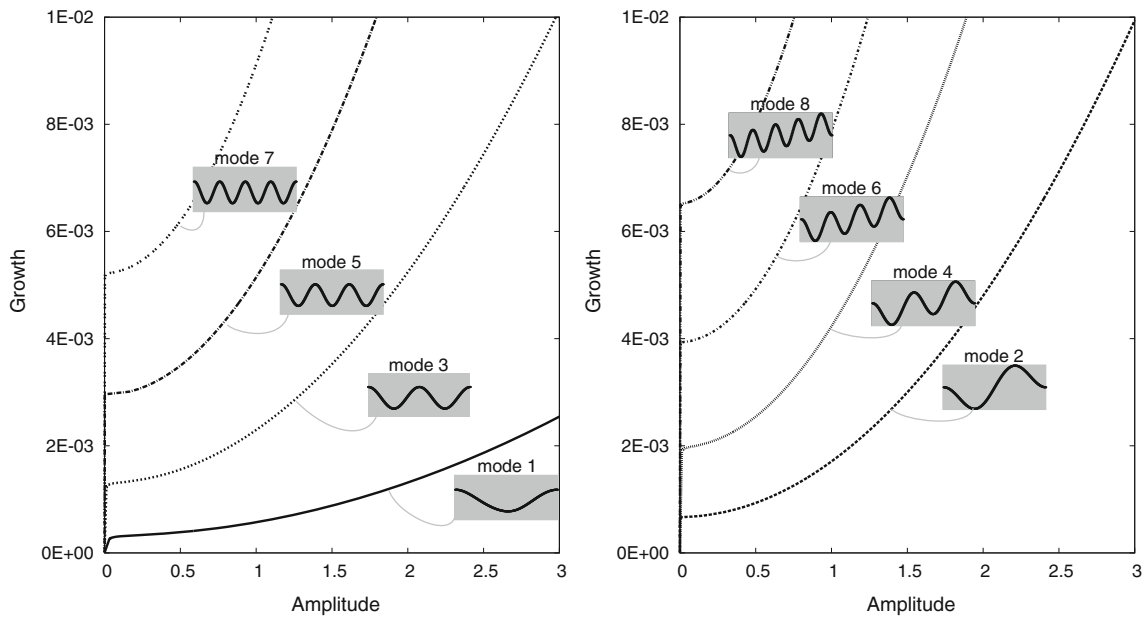


**Fig. 9** Bifurcation tree of the Euler beam computed by *perturbation analysis* using the information obtained from eigenvalue analysis

ments. Third, increasing the number of elements along the beam improves the convergence for both  $\nu = 0$  and  $\nu = 0.49$ . Fourth, for Poisson’s ratio  $\nu = 0$ , increasing the number of elements along the beam eventually converges towards the analytical solution regardless of the number of elements across the thickness. However, this behavior is not observed for  $\nu = 0.49$ . The numerical solution for  $\nu = 0.49$  can only converge to the analytical one if there are enough elements along as well as across the specimen. Finally, For Poisson’s ratio  $\nu = 0$ , increasing the number of elements across the thickness does not improve the convergence behavior but, it has a strong influence for  $\nu = 0.49$ . This involves even more elements. However, the error associated with linear elements is by far more than that of the quadratic ones for the same number of elements. For instance, for  $\nu = 0.49$  even 12 quadratic elements (142 DOFs) are more accurate than 48000 linear elements (107998 DOFs). It is well-known that in the incompressibility limit  $\nu \rightarrow 0.5$  classical quadratic elements show locking behavior and mixed, enhanced, or stabilized formulations [23,33,44,50–52,60,62] shall be used.

**4.1.3 Bifurcation tree obtained by perturbation**

In the previous section, we have shown that the eigenvalue analysis furnishes a suitable method to study growth-induced instabilities. In particular, we have shown the poor performance of the linear elements compared to the quadratic elements. In this section we show that equipped with the information achieved from the eigenvalue analysis, we can establish sound studies by *prescribing perturbations*. In fact, the insight provided by eigenvalue analysis allows us to

capture higher instability modes through *prescribing perturbations* and eventually, to compute the complete bifurcation tree.

This study focuses on the bifurcation tree of the Euler beam. The perturbations of this examples are random forces applied at all nodes and in both directions of the order of magnitude  $1 \text{ e}^{-7}$ . The random perturbations are small enough such that the result does not depend on them. To confirm the insensitivity of the solution, we have increased and decreased the perturbation by an order of magnitude and have obtained the same results. We run each example 100 times, each time with a force perturbation randomly generated by the machine and we constantly obtain the same result. Prescribing a growth value in the vicinity of the critical growth from the eigenvalue analysis allows us to explore not only the first bifurcation mode, but also higher modes. Then running the simulations with small increments always results in the same local minima associated with the eigenmode of interest. We emphasize that this is only possible since our finite element solution is based on the stationarity condition and not on the global minimization. For instance, in the vicinity of the critical growth associated with the second mode the stiffness contains one negative eigenvalue and one eigenvalue very close to zero. The minimization of energy would be in favor of the solution with the negative eigenvalue and therefore, constantly results only in the first eigenmode. However, stationarity condition can capture local minima and the solution shows more sensitivity with respect to the eigenvalue close to zero rather than the negative one. Figure 9 shows the results of the computations using 120 quadratic elements. The results are split into odd modes and even modes for better clarity.

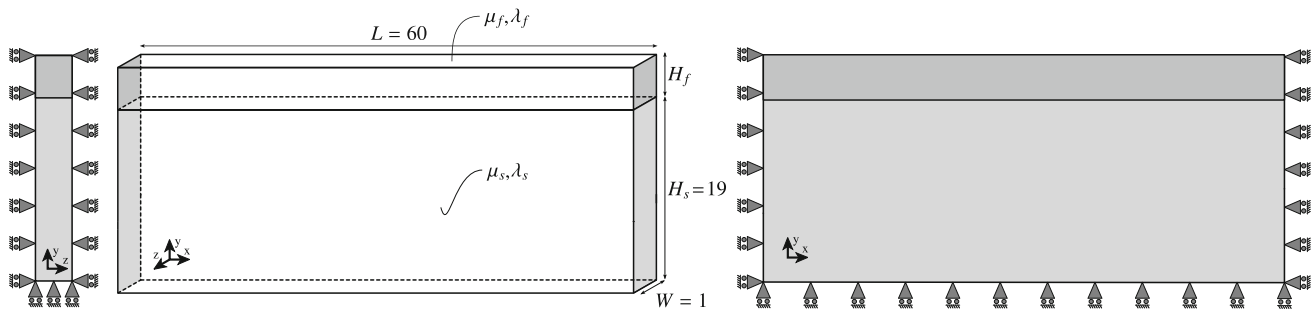


**Fig. 10** Instability study of a growing film on a soft substrate

## 4.2 Instability study of a growing film on a soft substrate

The next example of interest is the instability analysis of a thin growing film on a soft substrate constrained in a rectangular domain under plane-strain conditions. The geometry and boundary conditions of the problem are shown in Fig. 10. The domain has the length  $L = 60$  and width  $W = 1$ . The specimen consists of a substrate with the height  $H_s = 19$  on top of which the film with the thickness  $H_f$  is attached. We study this example for three different film thicknesses of  $H_f = 0.4$ ,  $H_f = 0.8$  and  $H_f = 1.2$ . The material properties of the substrate are fixed as  $\mu_s$  and Poisson's ratio of  $\nu_s = 0.49$ . The Poisson's ratio of the film is also,  $\nu_f = 0.49$ . We vary the film stiffness such that  $\mu_f/\mu_s$ , referred to as *stiffness ratio*, assumes different values from 4 to 900. The film grows isotropically and the substrate does not grow, at all. The domain is discretized using 840 bi-quadratic elements along the length with 19 elements in the height direction of the substrate. We have explored the influence of the number of elements across the film thickness and concluded that using quadratic elements, the number of elements across the film does not play a noticeable role. Also, the dimensions of the domain are arbitrarily chosen and clearly, do not represent the infinity assumptions associated with the theoretical solution of this problem [1,6].

Figure 11 summarizes the results of the eigenvalue analysis for several simulations. In particular, the critical growth  $g_c$  to initiate instabilities as well as the number of folds  $N$  associated with  $g_c$  are illustrated versus different stiffness ratios  $\mu_f/\mu_s$ . Note that  $N$  will always be a multiple of 0.5 due to the prescribed boundary conditions. Furthermore, we calculate the wavelength  $\lambda = L/N$  and plot it versus the cubic root of the stiffness ratio. The graphs of Fig. 11 show the common conclusions [see for instance [6]] briefly stated as follows.

First, Increasing the stiffness ratio decrease the critical growth  $g_c$ . For a softer substrate the film needs less growth to overcome the stiffness of the substrate and to fold. Second, for a given stiffness ratio, increasing the thickness does not change the critical growth. Third, the number of folds

decreases for increasing stiffness ratio. Fourth, increasing the film thickness reduces the number of folds. Finally, the wave length is proportional to the cubic root of the stiffness ratio.

## 4.3 Three dimensional example

This section proves the applicability of the eigenvalue analysis for three dimensional problems. The domain of interest consist of a thin growing film on a soft substrate as shown in Fig. 12. The radius of the cylinder is  $R = 30$  and the height of the substrate is chosen as  $H_s = 19$ . We study the influence of the film thickness by varying it as  $H_f = 1.0$ , 1.2, 1.5. The substrate is fixed in the  $y$  direction at the bottom and is fixed in  $x$  and  $z$  direction on the walls of the domain. This is equivalent to fix the walls in the radial and circumferential directions.

Both substrate and film are assumed to be fully compressible and therefore,  $\nu_s = \nu_f = 0$ . The stiffness ratio of the film over the substrate is chosen as  $\mu_f/\mu_s = 50, 100, 200, 500, 1000$ . The film is growing isotropically until it causes geometric instabilities in the forms of folding on the surface. Table 1 gathers the critical growth values for different thicknesses and different stiffness ratios.

Figures 13 and 14 illustrate the isometric view for all different thicknesses and stiffness ratios. We emphasize that this study is carried out using solely the eigenvalue analysis and therefore, the patterns observed in Figs. 13 and 14 are not the actual deformations. Solving this problem with *prescribing perturbation*, however, will lead to deformations similar to the modes predicted by the eigenvalue analysis. The main advantage of eigenvalue analysis is that this result is obtained robustly and repeatedly, without any artificial perturbations. Furthermore, the eigenvalue analysis calculates the critical growth precisely. This three-dimensional study leads to the following conclusions in agreements with our findings from the two-dimensional study in Sect. 4.2.

First, increasing the stiffness ratio decrease the critical growth  $g_c$ . Second, for a given stiffness ratio, increasing the thickness has a minor effect on the critical growth. The

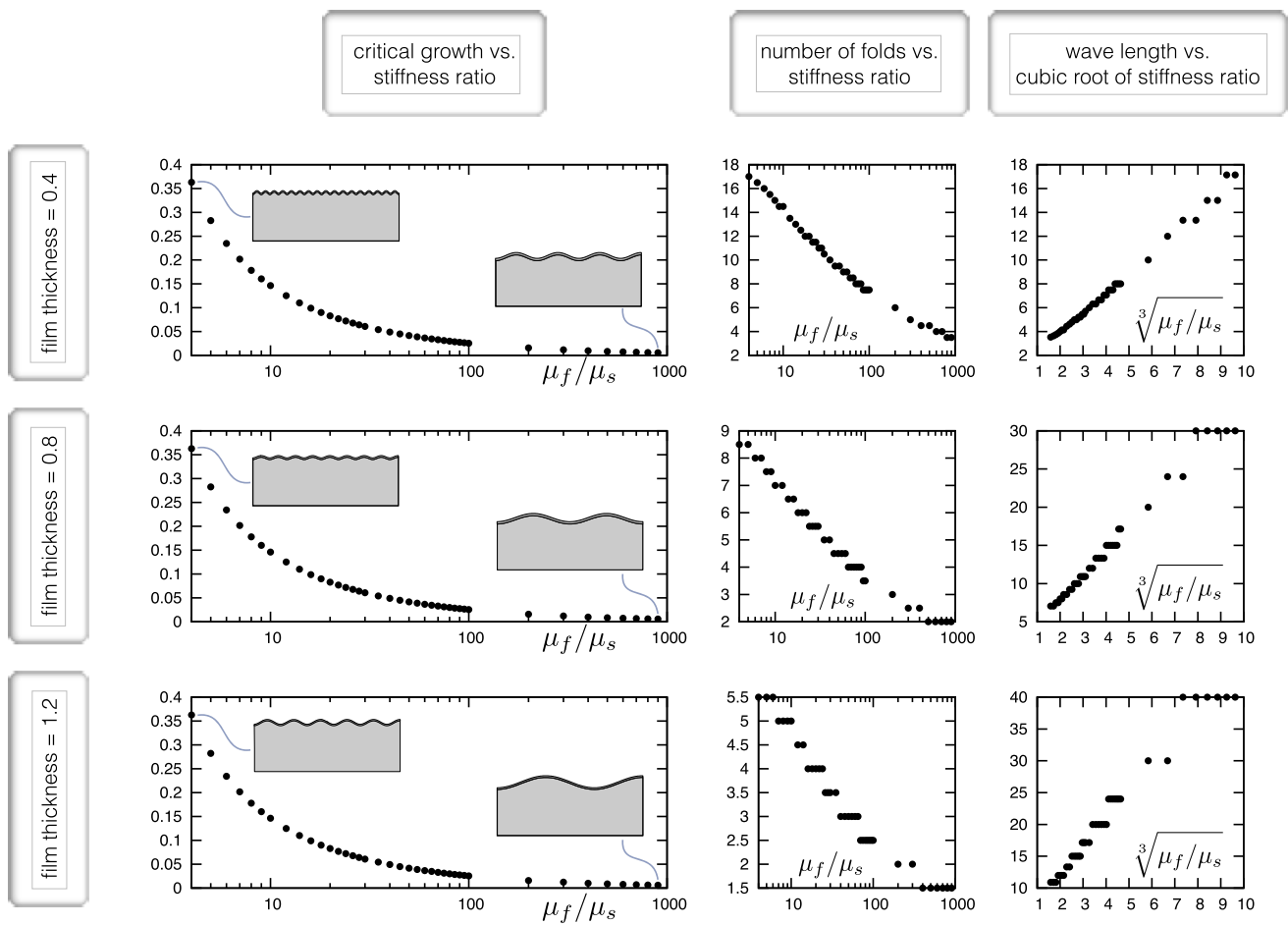


**Fig. 11** Instability study of a growing film on a soft substrate. The stiffness ratio of the film over the substrate is denoted as  $\mu_f/\mu_s$  and Poisson’s ratio for both the film and the substrate is  $\nu_f = \nu_s = 0.49$

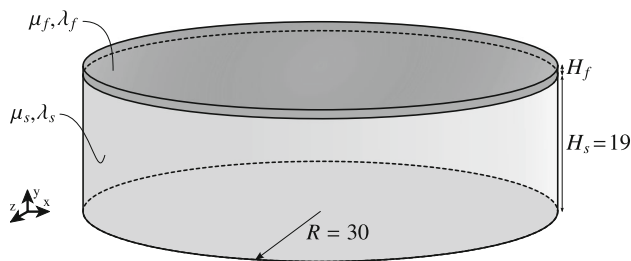


**Fig. 12** Instability study of a growing film on a soft substrate for a cylindrical geometry by eigenvalue analysis

analytical solution of this problem [1] suggests that the critical growth does not depend on the film thickness. However, we observe a minor influence of the thickness on the critical growth. This small discrepancy seems reasonable since the analytical solution is based on an infinite half-space, but the finite element model is only an approximation to that. When increasing the film thickness, we require more growth to buckle to overcome the film’s own thickness. Third, the wavelength increases for increasing stiffness ratio. Finally, increasing the film thickness reduces the number of folds.

### 5 Concluding remarks

The growth in bio-materials and living systems is often the origin for geometric instabilities in the form of folding or wrinkling. To better understand this phenomenon, it is important to know when and how these instabilities form. Here we have presented our first attempts to systematically identify the critical conditions for growth-induced instabilities.

The accepted strategy to study growth-induced instabilities is to prescribe perturbations such as nodal displacements or forces. This strategy is essentially subjective as perturbations are prescribed by the user and the results largely depend on perturbations. The key idea of this manuscript is to replace this common strategy by an eigenvalue analysis and to establish a generic framework towards understanding growth-induced instabilities. The eigenvalue analysis is first, perturbation-independent and second, it is, independent of the time step size. Therefore, the solution obtained by this methodology is no longer subjective. Not only the results obtained by eigenvalue analysis are generic and reproducible,

**Table 1** The critical growth values to initiate instabilities for a growing film on a soft substrate with cylindrical geometry. The ratio  $\mu_f/\mu_s$  indicates the stiffness ratio of the film with respect to the substrate. The computations are carried out using eigenvalue analysis

	$\mu_f/\mu_s = 50$	$\mu_f/\mu_s = 100$	$\mu_f/\mu_s = 200$	$\mu_f/\mu_s = 500$	$\mu_f/\mu_s = 1000$
$H_f = 1.0$	60.12 e-3	35.45 e-3	21.77 e-3	11.79 e-3	8.01 e-3
$H_f = 1.2$	60.50 e-3	36.12 e-3	22.26 e-3	12.78 e-3	8.44 e-3
$H_f = 1.5$	61.44 e-3	37.02 e-3	23.43 e-3	13.52 e-3	8.80 e-3

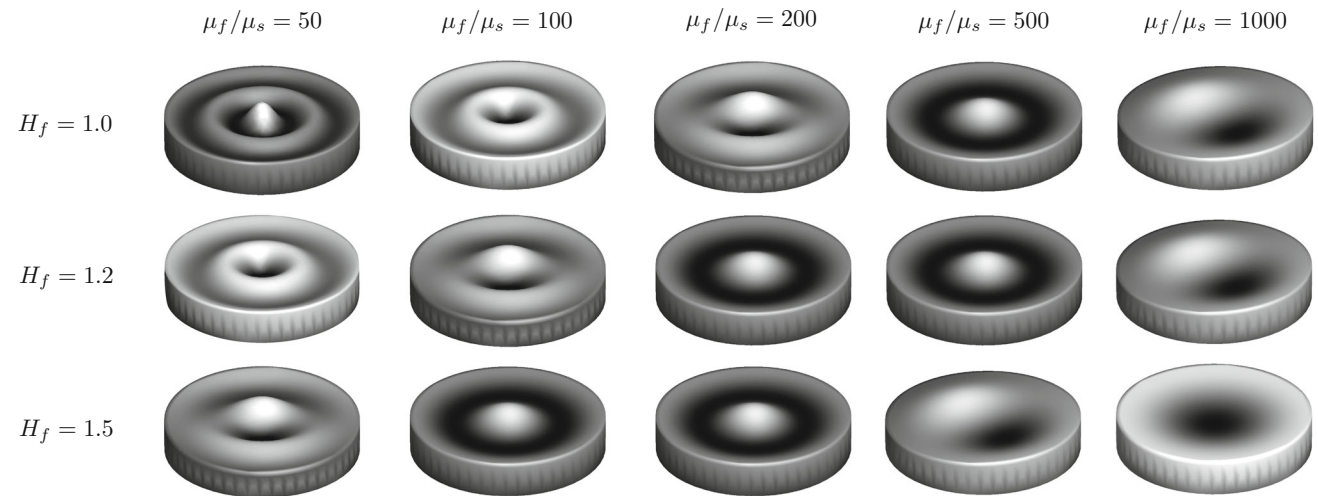


**Fig. 13** Instability study of a growing film on a soft substrate for a cylindrical geometry by eigenvalue analysis for different film thicknesses and different stiffness ratio

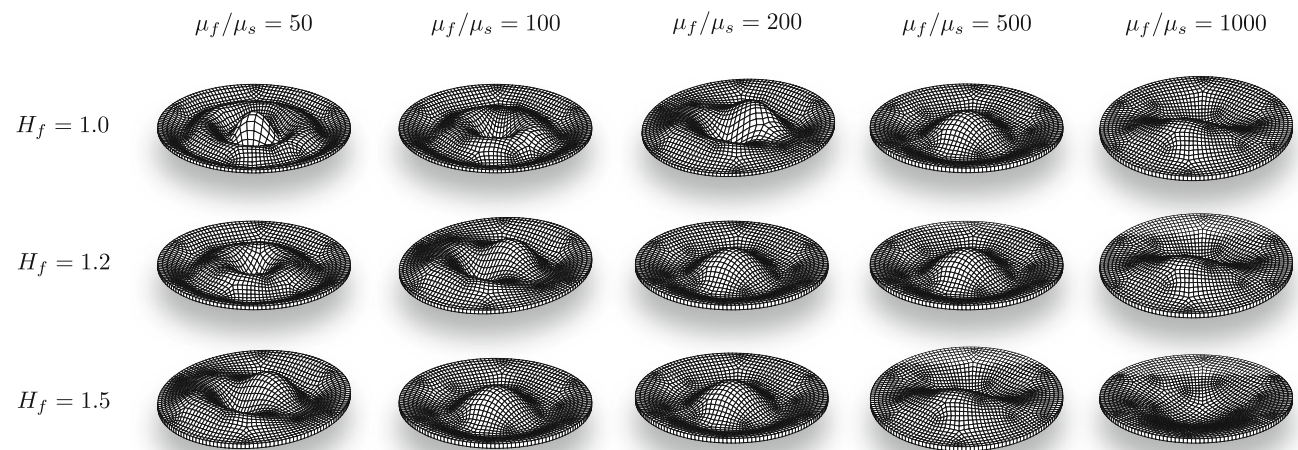


**Fig. 14** Instability study of a growing film on a soft substrate for a cylindrical geometry by eigenvalue analysis for different film thicknesses and different stiffness ratio. For clarity, the substrate is removed and the perspective view differs from Fig. 13

but also, for a given accuracy, this strategy can be computationally more than 100 times more efficient than prescribing perturbations. Using the eigenvalue analysis, we are able to compute precisely the critical growth to initiate instabilities. Equipped with this powerful tool, we then compare different

finite elements. Our results clearly, suggest to use quadratic elements for this family of problems.

Our next immediate plan is to compare the performance of other classical finite elements and more sophisticated enhanced finite element formulations. In particular, we aim

to introduce a new class of enhanced finite element suitable for growth and growth-induced instabilities in the incompressibility limit. Further extensions of this work include studying the challenging problem of period-doubling and period-tripling in growing bilayered systems [see [7], among others].

In summary, this manuscript presents our first attempt to shed light on growth-induced instabilities by eigenvalue analysis. This allows us to precisely predict the critical growth levels at which morphological instabilities may occur. We believe that this generic framework is broadly applicable to enhance our understanding of growth-induced instabilities with a large variety of applications in soft bio-materials and living systems.

**Acknowledgments** Financial support was provided by Samsung Electronics and the James M. Gere Research Fellowship from Stanford University. This support is gratefully acknowledged.

## References

- Allen HG (1969) Analysis and design of structural sandwich panels. Pergamon Press, New York
- Bathe KJ (2013) The subspace iteration method—revisited. *Comput Struct* 126:177–183
- Bathe K-J, Wilson EL (1973) Solution methods for eigenvalue problems in structural mechanics. *Int J Numer Methods Eng* 6:213–226
- Ben Amar M, Goriely A (2005) Growth and instability in elastic tissues. *J Mech Phys Solids* 53:2284–2319
- Biot MA (1957) Folding instability of a layered viscoelastic medium under compression. *Proc R Soc A* 242:444–454
- Biot MA (1965) Mechanics of incremental deformation. Wiley, New York
- Budday S, Kuhl E, Hutchinson JW (2015) Period-doubling and period-tripling in growing bilayered systems. *Philos Mag*. doi:10.1080/14786435.2015.1014443
- Budday S, Steinmann P, Kuhl E (2014) The role of mechanics during brain development. *J Mech Phys Solids* 72:75–92
- Cao Y, Hutchinson JW (2012a) From wrinkles to creases in elastomers: the instability and imperfection-sensitivity of wrinkling. *Proc R Soc A* 468:94–115
- Cao Y, Hutchinson JW (2012b) Wrinkling phenomena in Neo-Hookean film/substrate bilayers. *J Appl Mech* 79:031019
- Ciarletta P, Balbi V, Kuhl E (2014) Pattern selection in growing tubular tissues. *Phys Rev Lett* 113:248101
- Ciarletta P, Maugin GA (2011) Elements of a finite strain-gradient thermomechanical theory for material growth and remodeling. *Int J Non-Linear Mech* 46:1341–1346
- Ciarletta P, Preziosi L, Maugin GA (2013) Mechanobiology of interfacial growth. *J Mech Phys Solids* 61(3):852–872
- Cowin SC, Hegedus DH (1976) Bone Remodeling. 1. Theory of Adaptive Elasticity. *J Elast* 6(3):313–326
- Dervaux J, Ben Amar M (2011) Buckling condensation in constrained growth. *J Mech Phys Solids* 59(3):538–560
- Dervaux J, Ciarletta P, Ben Amar M (2009) Morphogenesis of thin hyperelastic plates: a constitutive theory of biological growth in the Föppl-von Kármán limit. *J Mech Phys Solids* 57:458–471
- Dunlop JWC, Fischer FD, Gamsjäger E, Fratzl P (2010) A theoretical model for tissue growth in confined geometries. *J Mech Phys Solids* 58:1073–1087
- Ehret AE (2015) On a molecular statistical basis for Ogden’s model of rubber elasticity. *J Mech Phys Solids* 78:249–268
- Epstein M, Maugin GA (2000) Thermomechanics of volumetric growth in uniform bodies. *Int J Plast* 16:951–978
- Eskandari M, Pfaller MR, Kuhl E (2013) On the role of mechanics in chronic lung disease. *Materials* 6:5639–5658
- Garikipati K, Arruda EM, Grosh K, Narayanan H, Calve S (2004) A continuum treatment of growth in biological tissue: the coupling of mass transport and mechanics. *J Mech Phys Solids* 52:1595–1625
- Genzer J, Groenewold J (2006) Soft matter with hard skin: from skin wrinkles to templating and material characterization. *Soft Matter* 2:310–323
- Glaser S, Armero F (1997) On the formulation of enhanced strain finite elements in finite deformations. *Eng Comput* 14:759–791
- Goriely A, Robertson-Tessi M, Tabor M, Vandiver R (2008) Elastic growth models. *Math Model Biosyst* 102:1–44
- Huang ZY, Hong W, Suo Z (2005) Nonlinear analyses of wrinkles in a film bonded to a compliant substrate. *J Mech Phys Solids* 53:2101–2118
- Hutchinson JW (2013) The role of nonlinear substrate elasticity in the wrinkling of thin films. *Philos Trans R Soc A* 371:20120422
- Javili A, Chatzigeorgiou G, Steinmann P (2013) Computational homogenization in magneto-mechanics. *Int J Solids Struct* 50:4197–4216
- Javili A, McBride A, Steinmann P (2013) thermomechanics of solids with lower-dimensional energetics: on the importance of surface, interface, and curve structures at the nanoscale. A unifying review. *Appl Mech Rev* 65(1):010802
- Javili A, Steinmann P, Kuhl E (2014) A novel strategy to identify the critical conditions for growth-induced instabilities. *J Mech Behav Biomed Mater* 29:20–32
- Jiang H, Khang DY, Fei H, Kim H, Huang Y, Xiao J, Rogers JA (2008) Finite width effect of thin-films buckling on compliant substrate: experimental and theoretical studies. *J Mech Phys Solids* 56:2585–2598
- Jin L, Cai S, Suo Z (2011) Creases in soft tissues generated by growth. *Europhys Lett* 95:64002
- Khang DY, Rogers JA, Lee HH (2009) Mechanical buckling: mechanics, metrology, and stretchable electronics. *Adv Funct Mater* 19:1526–1536
- Krischok A, Linder C (2015) On the enhancement of low-order mixed finite element methods for the large deformation analysis of diffusion in solids. *Int J Numer Methods Eng* (under review)
- Kuhl E, Menzel A, Steinmann P (2003) Computational modeling of growth. A critical review, a classification of concepts and two new consistent approaches. *Comput Mech* 32:71–88
- Kuhl E, Maas R, Himpel G, Menzel A (2007) Computational modeling of arterial wall growth. *Biomech Model Mechanobiol* 6:321–331
- Li B, Cao YP, Feng XQ, Gao H (2011) Surface wrinkling of mucosa induced by volumetric growth: theory, simulation and experiment. *J Mech Phys Solids* 59:758–774
- Li B, Cao Y-P, Feng X-Q, Gao H (2012) Mechanics of morphological instabilities and surface wrinkling in soft materials: a review. *Soft Matter* 8:5728
- Linder C, Tkachuk M, Miehe C (2011) A micromechanically motivated diffusion-based transient network model and its incorporation into finite rubber viscoelasticity. *J Mech Phys Solids* 59:2134–2156
- McBride AT, Javili A, Steinmann P, Bargmann S (2011) Geometrically nonlinear continuum thermomechanics with surface energies coupled to diffusion. *J Mech Phys Solids* 59(10):2116–2133

40. Menzel A, Kuhl E (2012) Frontiers in growth and remodeling. *Mech Res Commun* 42:1–14
41. Moulton DE, Goriely A (2011) Circumferential buckling instability of a growing cylindrical tube. *J Mech Phys Solids* 59(3):525–537
42. Nguyen DT (2008) Finite element methods: parallel-sparse statics and Eigen-solutions. Springer, New York
43. Ogden RW (1972) Large deformation isotropic elasticity: on the correlation of theory and experiment for incompressible rubberlike solids. *Proc R Soc Lond A* 326(1567):565–584
44. Panuso D, Bathe KJ (1995) A four-node quadrilateral mixed-interpolated element for solids and fluids. *Math Methods Models Appl Sci* 5:1113–1128
45. Papastavrou A, Steinmann P, Kuhl E (2013) On the mechanics of continua with boundary energies and growing surfaces. *J Mech Phys Solids* 61:1446–1463
46. Raina A, Linder C (2014) A homogenization approach for nonwoven materials based on fiber undulations and reorientation. *J Mech Phys Solids* 65:12–34
47. Raina A, Linder C (2015) A micromechanical model with strong discontinuities for failure in nonwovens at finite deformation. *Int J Solids Struct* (under review)
48. Richman DP, Stewart RM, Hutchinson JW, Caviness VS (1975) Mechanical model of brain convolitional development. *Science* 189:18–21
49. Rodriguez EK, Hoger A, McCulloch AD (1994) Stress-dependent finite-growth in soft elastic tissues. *J Biomech* 27(4):455–467
50. Simo JC, Rifai MS (1990) A class of mixed assumed strain methods and the method of incompatible modes. *Int J Numer Methods Eng* 29:1595–1638
51. Simo JC, Armero F (1992) Geometrically non-linear enhanced strain mixed methods and the method of incompatible modes. *Int J Numer Methods Eng* 33:1413–1449
52. Simo JC, Armero F, Taylor RL (1993) Improved versions of assumed enhanced strain tri-linear elements for 3D finite deformation problems. *Comput Methods Appl Mech Eng* 110:359–386
53. Sun J-Y, Xia S, Moon M-W, Oh KH, Kim K-S (2012) Folding wrinkles of a thin stiff layer on a soft substrate. *Proc R Soc A* 468:932–953
54. Taber LA (1995) Biomechanics of growth, remodeling, and morphogenesis. *Appl Mech Rev* 48:487–545
55. Tepole AB, Ploch CJ, Wong J, Gosain AK, Kuhl E (2011) Growing skin: a computational model for skin expansion in reconstructive surgery. *J Mech Phys Solids* 59:2177–2190
56. Timoshenko SP, Gere JM (1961) Theory of elastic stability. McGraw-Hill, New York
57. Tkachuk M, Linder C (2012) The maximal advance path constraint for the homogenization of materials with random network microstructure. *Philos Mag* 92:2779–2808
58. Wagner S, Lacour SP, Jones J, Hsu PHI, Sturm JC, Li T, Suo Z (2004) Electronic skin: architecture and components. *Phys E* 25:326–334
59. Wagner W, Wriggers P (1988) A simple method for the calculation of postcritical branches. *Eng Comput* 5:103–109
60. Joshua A, Borja RI (2008) Stabilized low-order finite elements for coupled solid-deformation/fluid-diffusion and their application to fault zone transients. *Comput Methods Appl Mech Eng* 197:4353–4366
61. Wriggers P (2008) Nonlinear finite element methods. Springer, Berlin
62. Wriggers P, Reese S (1996) A note on enhanced strain methods for large deformations. *Comput Methods Appl Mech Eng* 135:201–209
63. Wriggers P, Wagner W, Miehe C (1988) A quadratically convergent procedure for the calculation of stability points in finite element analysis. *Comput Methods Appl Mech Eng* 70:329–347
64. Xu F, Potier-Ferry M, Belouettar S, Cong Y (2014) 3D finite element modeling for instabilities in thin films on soft substrates. *Int J Solids Struct* 51(21–22):3619–3632
65. Yavari A (2011) A geometric theory of growth mechanics. *J Nonlinear Sci* 20:781–830